CuO nanosheets embedded on carbon microspheres as high-performance anode material in lithium-ion batteries

Xun Sun[†], Zhe Wang[†], Xinping Ai[*] and Jinping Zhou[*]

ABSTRACT   Because of its high capacity, availability, and environmental friendliness, copper oxide (CuO) is a desirable anode material for lithium-ion batteries (LIBs). However, due to low intrinsic electrical conductivity and enormous volume expansion during cycling, the capacity utilization and cycle stability of the CuO anode remain insufficient for battery applications. In this study, we design and fabricate a three-dimensional (3D) porous carbon@CuO composite (C@CuO) by *in situ* synthesis of CuO nanosheets directly on the internal and external walls of chitin-derived carbon microspheres. Benefiting from the hierarchical conductive framework of the carbon microspheres and a rational distribution of CuO nanosheets, the capacity utilization and structural stability of the CuO nanosheets are substantially improved during the charge/discharge process. Thus, the C@CuO microspheres as the anode material for LIBs demonstrate a high reversible capacity of 626 mA h g^{-1} at 100 mA g^{-1} with a capacity retention of ~93% over 200 cycles, a stable specific capacity of 553 mA h g^{-1} after 600 cycles even at a high current density of 1000 mA g^{-1}, and superior rate capability with a high discharge capacity of 262 mA h g^{-1} at 5000 mA g^{-1}. Therefore, this study innovatively constructs carbon microspheres with a hierarchical structure accompanied by self-growing CuO nanosheets as the anode material for LIBs, which may provide a new idea for the rational design of 3D carbon/metal oxide hybrids.

Keywords: chitin-derived carbon, microspheres, CuO nanosheets, hierarchical pore structure, anode material

INTRODUCTION

At present, lithium-ion batteries (LIBs) continue to dominate all battery systems because of their distinct features of long cycle life, high operating voltage, environmental compatibility, and high energy density [1–3]. Graphite is used as a commercial anode material for LIBs because of its chemical stability, abundance, and low cost [4]. However, because of the poor rate performance and the low theoretical capacity (~372 mA h g^{-1}) of graphite, the rising requirements in next-generation energy storage devices are difficult to fulfill [5,6]. Consequently, new anode materials with high energy storage potentials urgently need to be developed for LIBs. Much effort has been devoted to

searching for ideal anode materials to enhance the reversible storage capacity of lithium ions. Transition metal oxides, such as TiO$_2$ [7,8], Co$_3$O$_4$ [9–11], MnO$_2$ [12,13], NiO [14,15], Fe$_3$O$_4$ [16–18], SnO$_2$ [19,20], and CuO [2,21–24], are considered very attractive anode alternatives for high-performance LIBs and are being intensively studied because of their superior theoretical lithium-ion storage capacity compared with commercial graphite. In particular, CuO has gained considerable interest as a potential anode material to replace traditional graphite because of its reasonable cost, environmental friendliness, abundance, and high theoretical capacity (~670 mA h g^{-1}) [25–27]. Nevertheless, CuO still has many difficulties to overcome, including its large and uneven growth of volume while charging and discharging and its low intrinsic conductivity, which leads to poor cycle stability and substantial capacity loss [28,29].

To solve these problems, modifying the morphology of particles, optimizing their size, and creating carbon hybrids with acceptable nanostructures are considered effective methods. Several studies have demonstrated that the effective design and tuning of CuO morphology, such as nanosheets [30,31], nanorods [2,32], nanofibers [33], nanoflakes [34], nanowires [35,36], nanoparticles [5,22], and nanoplates [37], can help enhance the utilization of CuO and inhibit the volume expansion during the lithiation and de-lithiation processes. Nevertheless, most CuO-based anodes exhibit mediocre performance because of their poor electrical conductivity. In contrast, combining CuO with nanostructured carbon materials can increase the electrical conductivity of the electrodes, enhancing their electrochemical performance. Three-dimensional (3D) constructed porous carbon materials are considered the most promising substrates for LIBs because of their unique features, including a large specific surface area, a rich porous structure, and a modifiable pore size distribution [38]. The hierarchical porous structure (e.g., micro/meso/micropores) facilitates the penetration of electrolytes and the contact between the electrolyte and the electrode surface. In addition, the 3D interconnected pore network facilitates electron transfer along its backbone while promoting lithium-ion transport through interconnected nanopores and increasing the transfer rate of electrons and lithium ions, and this mixed charge conduction channel ensures high-rate performance [39,40]. Furthermore, the 3D interconnected pore network can improve the cycling

Hubei Engineering Center of Natural Polymer-based Medical Materials, Engineering Research Center of Organosilicon Compounds & Materials of Ministry of Education, Department of Chemistry, Wuhan University, Wuhan 430072, China

[†] These authors contributed equally to this work.

[*] Corresponding authors (emails: zhoujp325@whu.edu.cn (Zhou J); xpai@whu.edu.cn (Ai X))

stability of LIBs by buffering the volume expansion of electrodes during the charge/discharge process [28]. For example, Pu et al. [41] reported the reduced graphene oxide (RGO) loaded with CuO ultrathin nanosheets as an anode for LIBs and confirmed that wrinkled RGO layers combined with CuO nanosheets via interfacial coupling exhibited excellent rate capability and high reversible capacity. Chen et al. [5] successfully prepared activated tubular carbon loaded with ultrafine CuO nanoparticles as an anode material for LIBs. The obtained carbon/CuO nanosheet electrode exhibited enhanced rate capability and cycling stability due to the co-effect of the unique microporous structure, large specific surface area, and the abundant oxygen-containing groups of the activated tubular carbon. However, the weak contact between the conductive additive and the CuO nanostructures leads to their segregation during the lithiation and de-lithiation processes, particularly resulting in low electrochemical activity at high current densities [42,43]. Therefore, constructing reasonable CuO morphologies while combining them with conductive carbon remains a difficult task.

In terms of sustainability, biomass pyrolysis has become one of the most extensively used, cost-effective, and environmentally friendly methods for producing porous carbon-based materials for energy storage [44–47]. Chitin, which has a high proportion of N/O functional groups, is the second most prevalent source of biomass on the planet. The direct pyrolysis of chitin enables the uniform integration of heteroatoms into a carbon structure, resulting in N, O self-doped carbon. Chitin has enormous promise as an ideal precursor to produce nanostructured carbon-based anode materials for LIBs [48]. In this study, we inventively built a porous carbon microsphere (CM) derived from chitin with a dense growth of CuO nanosheets as a highly efficient anode material in LIBs. First, the obtained CMs, coated with nearly vertically aligned and interlaced CuO nanosheets, exhibit a unique structure, which can lead to excellent electrochemical properties. The multiscale porous structure and the effective space between adjacent CuO nanosheets not only enable a large electrode/electrolyte interface for rapid reactions but also can accommodate the volume change during cycling. Second, the interlaced CuO nanosheets formed directly on the carbon substrates are structurally stable, thereby reducing the pulverization during cycling, which is advantageous for structural integrity. Finally, the nitrogen-doped carbon substrate and CuO nanosheets may promote the uniform nucleation and homogeneous growth of Li, hence enhancing the cycling stability of the electrode. With the co-effect of the hierarchical structure of CMs and the interlaced CuO nanosheets, the hybrid materials exhibit extraordinary potential in LIBs, delivering high reversible capacities and excellent long-term cycling stability and rate capabilities. This study developed a method for achieving homogeneous mixing between chitin chains and copper hydroxides, obtained homogenous carbon/copper hybrids after carbonization, and finally performed oxidation to CuO using a hydrothermal reaction to obtain carbon/CuO composite microspheres. The obtained carbon/CuO microspheres can ensure strong bonding between CuO and the substrate, providing a new idea for preparing carbon-based hybrid materials.

EXPERIMENTAL SECTION

Raw materials

Chitin was obtained from Golden Shell Biochemical Co., Ltd.

(Zhejiang, China) and purified as previously described [49]. $Cu(OH)_2$ was purchased from Aladdin Biochemical Technology Co., Ltd. (Shanghai, China). All other chemicals were purchased from Sinopharm Chemical Reagent Co., Ltd. (Shanghai, China) and were of analytical grade.

Preparation of chitin@$Na_2[Cu(OH)_4]$ solution

NaOH (25 g) was dissolved in 30 mL of water and then cooled to 0°C in an ice-water bath. $Cu(OH)_2$ (5 g) was added and stirred for 5 min. A 10-mL aliquot of 5 wt% NaOH solution was then added and stirred for another 5 min. $Na_2[Cu(OH)_4]$ solution was obtained after standing for a few minutes to remove the precipitates. The purified chitin powders (12 g) were dispersed in 113 g of $NaOH/urea/H_2O$ (5:8:100 by weight), and stirred for 15 min to obtain a uniformly dispersed suspension. $Na_2[Cu(OH)_4]$ solution (70 g) was added to this suspension and mixed well under stirring. The obtained suspension was frozen at −40°C for 5 h and then thawed at ambient temperature, and chitin@$Na_2[Cu(OH)_4]$ solution was obtained after freezing–thawing several times.

Preparation of chitin@$Cu(OH)_2$ microspheres

A three-neck flask was filled with 100 mL of pre-mixed iso-pentane and 10 mL of Span 85 mixture and stirred at 1000 r min^{-1} for 30 min at 0°C. Then, the chitin@$Na_2[Cu(OH)_4]$ solution was added dropwise to this suspension. After stirring for 1 h, the reaction temperature was increased to 90°C, and stirred for another 1 h to obtain regenerated chitin@$Cu(OH)_2$ microspheres. The microspheres were washed repeatedly with 90% ethanol to remove the residual impurities and finally freeze-dried after solvent exchange with tert-butyl alcohol.

Preparation of C@CuO microspheres

The obtained chitin@$Cu(OH)_2$ microspheres were calcined at 800°C in an argon atmosphere for 2 h. Brown powder was obtained after carbonization, washed with deionized water, and then dried in a vacuum at 60°C for 24 h to obtain C@Cu microspheres. A certain number of C@Cu microspheres, 6 mL H_2O_2 (30%), 45 mL deionized water, and 0.96 g NaOH were added to a beaker and stirred for 8 h. Next, the mixture was transferred into a poly(tetrafluoroethylene) (Teflon)-lined autoclave (100 mL) and kept sealed under 110°C for 12 h. After the hydrothermal reaction, the reactor was naturally cooled to room temperature, and the C@CuO microspheres were collected, washed repeatedly with deionized water, and then dried at 60°C under vacuum.

The C@CuO microspheres were calcined in a muffle furnace at 400°C for 3 h to obtain bare CuO microspheres. The C@CuO microspheres were washed with a hydrochloric acid solution to remove CuO and obtain bare CMs.

Characterizations

Powder X-ray diffraction (XRD, XRD-6000, Cu Kα radiation of λ = 0.15406 nm, Japan), transmission electron microscopy (TEM, JEOLJEM-2010 (HT), Japan) equipped with an energy-dispersive X-ray spectrometer (EDS, Super-X), and scanning electron microscopy (SEM, FEI SIRION-200, USA) were used to characterize the structure and morphology of the samples. Surface elemental analysis was conducted using an X-ray photoelectron spectrometer (XPS, Escalab 250Xi, Thermo Fisher, USA). Thermogravimetric (TG) analysis was tested on a TA

Q500 instrument under an air atmosphere with a heating rate of 10°C min^{-1}. Raman spectroscopy was applied on an RM1000 spectrometer (Renishaw, UK). The nitrogen adsorption/desorption isotherms and pore size distributions of the samples were obtained on a Micromeritics ASPA 2020 analyzer (Micromeritics Instruments Corporation, USA).

Electrochemical measurements

Active materials (C@CuO, CMs, and bare CuO), polyacrylic acid, and Super P were mixed in deionized water in a mass ratio of 70:20:10 to produce a slurry in which the mass of the active material was approximately 1 mg. The slurry was then uniformly applied to copper foil using a sample maker and dried at 60°C for 12 h to produce the electrodes. The obtained electrodes, glass fiber membrane (GF/D, Whatman) as the separator, lithium metal foils with a thickness of 1 mm as the counter and reference electrodes, and 50 μL of LiPF$_6$ (1 mol L^{-1}) in a mixture of ethylene carbonate, dimethyl carbonate, and ethyl methyl carbonate (1:1:1 by volume) containing 10% fluoroethylene carbonate as the electrolyte were then assembled into a 2032-coin cell in an argon-filled glove box with less than 0.01 ppm of H$_2$O and O$_2$. The assembled cell was aged for at least 6 h before testing to ensure adequate electrolyte penetration into the electrodes. The galvanostatic charge/discharge (GCD) curves were measured at 0.01–3 V using a LAND-CT2011A battery measurement system. Electrochemical impedance spectroscopy (EIS) and cyclic voltammogram (CV) measurements were performed on an electrochemistry workstation (CHI660E, Shanghai Chenhua, China). EIS was evaluated at frequencies ranging from 0.01 Hz to 100 kHz, and the CV measurements were evaluated at a scan rate of 0.2–5 mV s^{-1} at 0.01–3 V. All electrochemical measurements were conducted at 25°C.

RESULTS AND DISCUSSION

Synthesis and structural characterization

The C@CuO microspheres with porous structures as high-performance anode materials for Li-ion batteries were fabricated by pyrolyzing the chitin@Cu(OH)$_2$ microspheres followed by a hydrothermal reaction (Scheme 1). The present study is based on the alkali/urea dissolution system, and a novel dissolution method has been developed. The Na$_2$[Cu(OH)$_4$] solution was prepared by first dissolving Cu(OH)$_2$ in a highly concentrated NaOH solution. Then, a certain concentration of alkali/urea solution was added to obtain a stable Na$_2$[Cu(OH)$_4$]/NaOH/urea system. Finally, chitin was dissolved in this system to achieve a homogeneous mixture of polymeric chains and Na$_2$[Cu(OH)$_4$]. The obtained chitin solution was added to the oil phase, and numerous spherical droplets were obtained by vigorous stirring and emulsion separation. The subsequent boiling water bath not only regenerated the chitin microspheres but also converted the Na$_2$[Cu(OH)$_4$] into Cu(OH)$_2$ because of the instability of Na$_2$[Cu(OH)$_4$] at high temperatures, thus obtaining chitin@Cu(OH)$_2$ microspheres. The XRD pattern of chitin@Cu(OH)$_2$ microspheres is shown in Fig. S1a. Because of the weak characteristic diffraction peaks of Cu(OH)$_2$ and overlap with those of chitin, only the distinctive diffraction peak of chitin was observed [50]. After lyophilization, the chitin@Cu(OH)$_2$ microspheres were carbonized in an argon atmosphere at 800°C, during which a series of pyrolysis and reduction reactions were
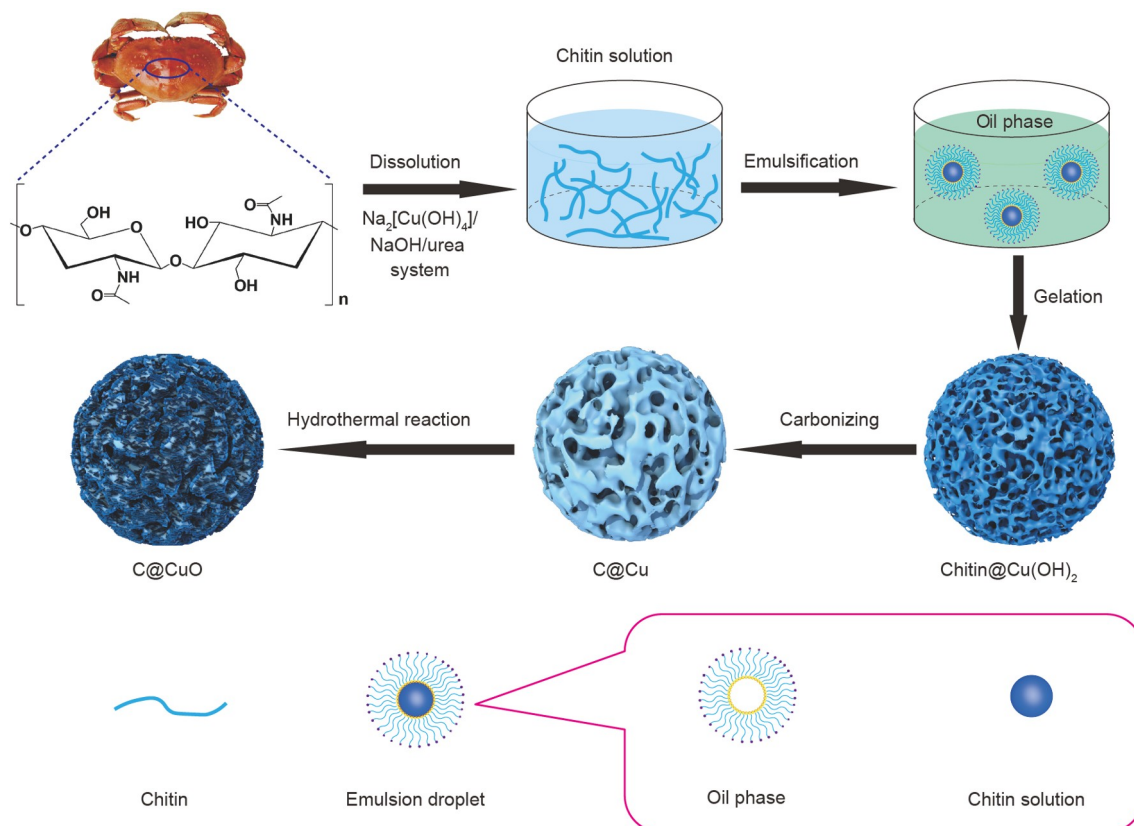
Scheme 1 Schematic illustration for the preparation of C@CuO microspheres.

carried out to finally produce C@Cu microspheres [22]. Then, the Cu was oxidized by the hydrothermal reaction, and C@CuO microspheres were obtained. All chitin@Cu(OH)$_2$ microspheres were spherical with an average diameter of 75 ± 5 μm and showed a porous structure on the surface (Fig. 1a). The cross-sectional SEM image of the chitin@Cu(OH)$_2$ microsphere showed a porous structure with internal and external interpenetrations (Fig. S1b). After carbonization at 800°C in argon, the obtained C@Cu microspheres remained spherical with an average diameter of 38 ± 10 μm and showed a more abundant porous structure (Fig. 1b). After the hydrothermal reaction, the Cu in the C@Cu microspheres was completely converted into CuO, and the size of the obtained C@CuO microspheres decreased further to 25 ± 5 μm. In the SEM images (Fig. 1c and Fig. S2), dense CuO nanosheets can be observed on the surface of the microspheres. In addition, the SEM cross-sectional view of C@CuO microspheres (Fig. S3) shows that many CuO nanosheets are distributed on the carbon walls. Thus, the CuO nanosheets were not only uniformly arranged on the surface but also grown on the carbon walls of the microspheres. Additionally, the growth of CuO nanosheets did not destroy the porous structure of the microspheres, and the interior of the C@CuO microspheres still had a rich porous structure, which was also demonstrated in the TEM image (Fig. 1d). From Fig. 1d, we see some CuO nanosheets at the edges of the microspheres. In the high-resolution TEM (HRTEM) image of CuO nanosheets

shown in Fig. 1e, we clearly observe the lattice fringes, and the distinct lattice spacing between two adjacent planes was calculated to be 0.231 nm, which can be ascribed to the (200) lattice plane of CuO. The mapping images of C@CuO were analyzed using high-angle annular dark-field scanning TEM equipped with EDS (HAADF-STEM-EDS) (Fig. 1f–j), and the mapping of C, N, O, and Cu elements can be clearly observed in the selected region.

Fig. 2a, b show the SEM images of the CMs. The CuO nanosheets have been completely removed, and the porous structure of the microspheres has not been destroyed. XRD and XPS characterizations further demonstrate that no CuO residue was on the CMs (Fig. 2c and Fig. S4). In Fig. 2d, e, SEM images show that bare CuO is composed of stacked CuO nanosheets. Moreover, the XRD pattern of bare CuO demonstrates the absence of carbon residues (Fig. 2f). Fig. 3a shows the XRD patterns of the C@Cu and C@CuO microspheres. The distinguishable diffraction peaks of C@Cu at 43.4°, 50.4°, and 74.1° are attributed to the (111), (200), and (220) crystal planes of Cu (PDF#70-3039), respectively. Herein, chitin served as the carbon source for the high-temperature reduction of Cu(II). Moreover, chitin and the extracted carbon worked as a substrate to prevent Cu nanoparticle aggregation [51]. For C@CuO microspheres, the diffraction peaks at 32.5°, 35.5°, 38.7°, 48.8°, 53.5°, 58.3°, 61.6°, 66.2°, and 68.1° are attributed to the (110), (002), (200), (20−2), (020), (202), (11−3), (022), and (220) planes of CuO
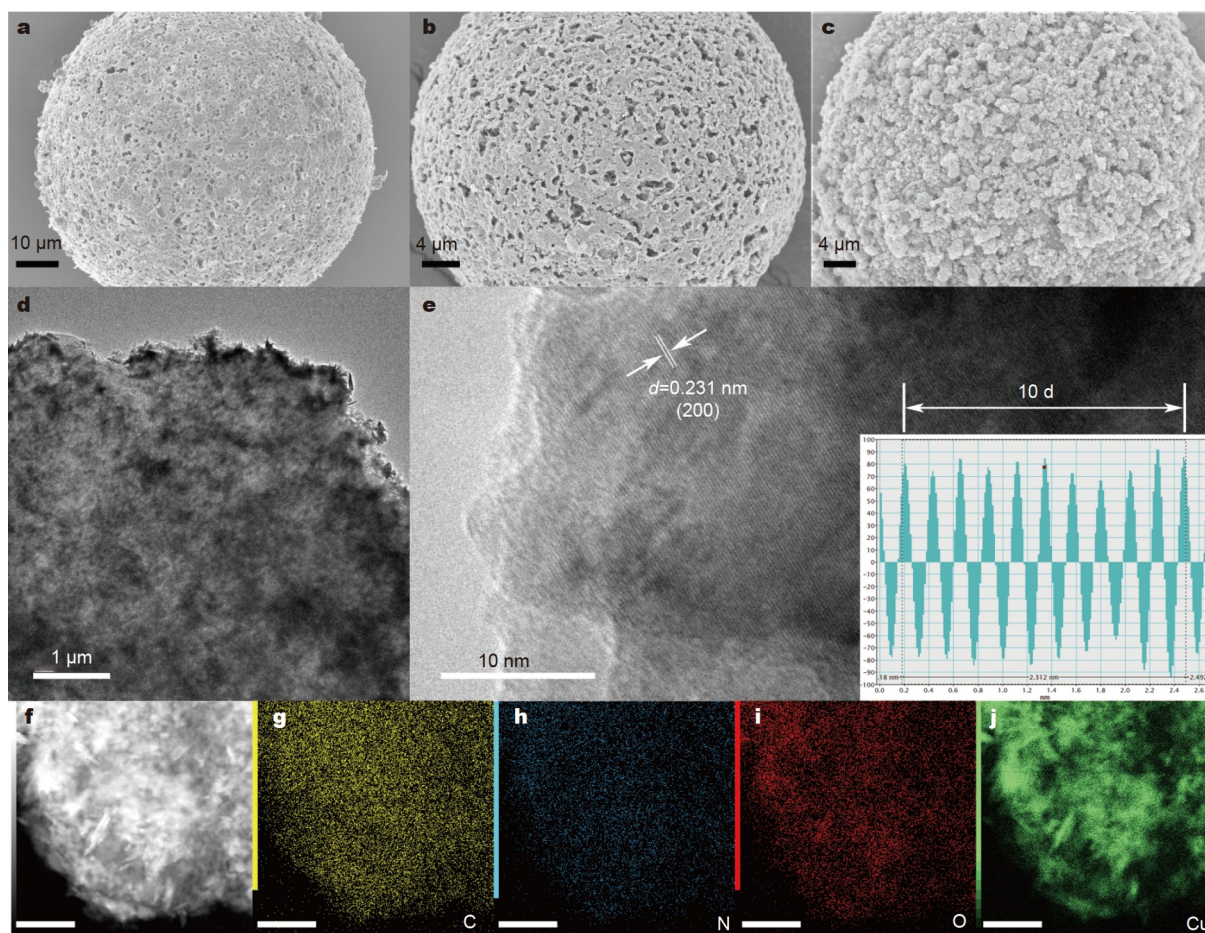

Figure 1 SEM images of (a) chitin@Cu(OH)$_2$, (b) C@Cu, and (c) C@CuO. (d) TEM and (e) HRTEM images of C@CuO (inset: line scan intensity profile across the lattice fringes). (f) HAADF-STEM image and (g–j) the corresponding EDS mapping of C@CuO. The scale bars are 250 nm.
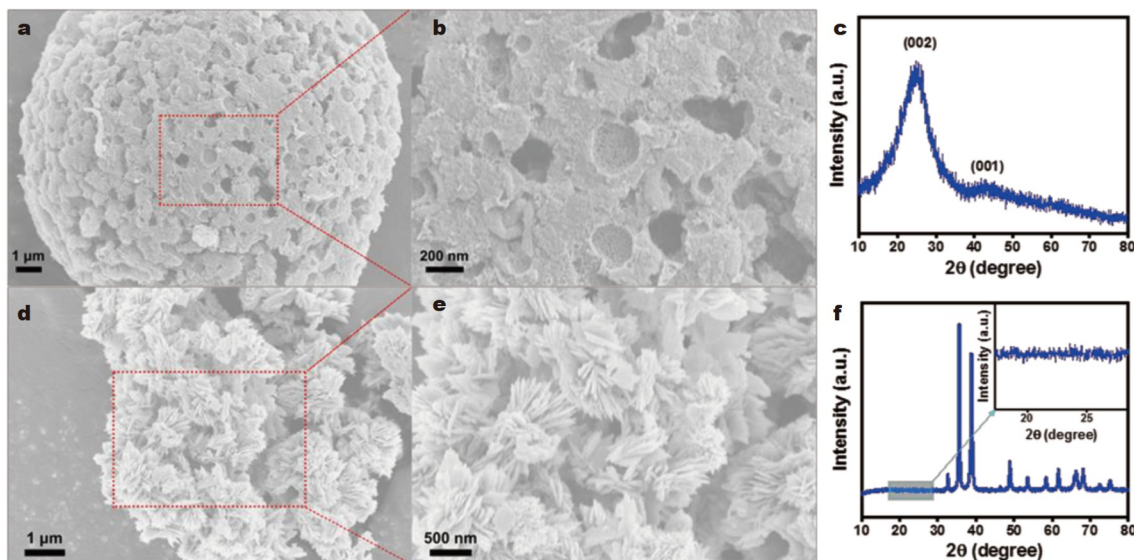
Figure 2   (a, b) SEM images and (c) XRD pattern of CMs. (d, e) SEM images and (f) XRD pattern of the bare CuO microspheres.

(PDF#45-0937), respectively, and all the diffraction peaks of Cu disappeared. This result shows that the Cu in the microspheres was completely converted to CuO, and the C@CuO microspheres were successfully prepared. Fig. 3b illustrates the TG and derivative TG (DTG) curves of the C@CuO microspheres in the air atmosphere. The main weight loss of the sample occurred in the range of 350–470°C. The carbon was gradually burned off in the air during this phase. In addition, some CuO was reduced to Cu_2O and Cu by carbon [52]. When all the carbon was burned, Cu_2O and Cu were then oxidized to CuO by O_2. By calculating the residue content in the TG curve, the amount of CuO in C@CuO microspheres was estimated to be 50.7 wt%. The DTG curve shows that the maximum weight loss rate of C@CuO microspheres occurred at approximately 400°C, providing the basis for the oxidation temperature in the preparation of bare CuO.

Fig. 3c shows the full-survey XPS spectrum of the C@CuO microsphere. The distinct peaks of C 1s, O 1s, N 1s, and Cu 2p confirm the presence of C, O, N, and Cu elements, respectively. The high-resolution XPS spectrum of C 1s (Fig. 3d) can be divided into C–C (284.8 eV), C–N/C–O (285.9 eV), and C=O (289.9 eV) bonds, respectively [53]. Fig. 3e displays the high-resolution XPS spectrum of N 1s, with the three peaks at binding energies of 398.5, 401.0, and 404.7 eV corresponding to pyridinic N, pyrrolic N, and graphitic N, respectively [54]. In the high-resolution O 1s spectrum (Fig. 3f), the peaks at the binding energies of 529.9, 531.3, and 532.7 eV are assigned to C=O, Cu–O, and C–O/C–OH, respectively [5]. Fig. 3g shows the high-resolution Cu 2p XPS spectra of C@CuO and the mixture of CMs and bare CuO. For C@CuO, two spin-orbiting doublets and two shakeup satellites can be observed. The two peaks at binding energies of 934.2 and 954.0 eV correspond to Cu $2p_{3/2}$ and Cu $2p_{1/2}$ of CuO nanosheets, respectively. The three satellite peaks at 941.6, 944.1, and 962.4 eV represent the shakeup peaks of Cu at the high binding energy sites of Cu $2p_{3/2}$ and Cu $2p_{1/2}$, respectively [2,23]. Therefore, the XRD and XPS results strongly suggest that CuO nanosheets were successfully generated on the carbon substrates. For the mixture of CMs and bare CuO, the peaks located at 933.5 and 953.6 eV can be attributed to Cu $2p_{3/2}$

and Cu $2p_{1/2}$, respectively, and are 0.7 and 0.4 eV lower than those of C@CuO, respectively. The increased binding energy of C@CuO indicates a decrease in electron density at the Cu sites, and the positive shift can be ascribed to the Cu–O–C bond formed between the CuO nanosheets and carbon substrate [55,56]. Furthermore, the nitrogen adsorption–desorption curves were measured to analyze the specific surface areas and pore size distributions of C@CuO and CMs (Fig. 3h, i and Table S1). All adsorption–desorption curves exhibit a clear hysteresis loop between the P/P_0 values of 0.4–1.0, indicating a typical type IV isotherm. The substantial increases in nitrogen adsorption by C@CuO and CMs at the relative pressures of P/P_0 < 0.1 and P/P_0 > 0.9 indicate the presence of a certain amount of micro- and macro-pores, respectively. Meanwhile, the presence of mesopores is evidenced by the hysteresis phenomenon at $0.4 < P/P_0 < 1.0$ [57,58]. The specific surface areas of C@CuO and CMs are 398.1 and 714.6 m^2 g^{-1}, respectively, and the corresponding pore volumes are 0.42 and 1.21 cm^3 g^{-1}, respectively. The pore size distribution calculated by the density functional theory (DFT) method indicates that micro- and meso-porous structures predominated in C@CuO and CMs, with average pore sizes of 0.55 and 0.60 nm, respectively. The 3D multiscale pore structure provides an interconnected carbon skeleton and a large specific surface area, which helps accommodate the large volume variation, enhance electronic conductivity, and facilitate ion transportation.

Electrochemical performance

Studies have shown that electrodes with a multiscale pore structure benefit LIBs, and we have evaluated the electrochemical performance of C@CuO as an anode material for LIBs. CV and GCD tests were conducted to assess their lithium storage capacity in lithium-ion half-cells. Fig. 4a shows the CVs of the C@CuO electrodes at a scan rate of 0.2 mV s^{-1}. Four reduction peaks were identified at 2.1, 1.23, 1.08, and 0.79 V in the first cathodic scan, which represented a multistep electrochemical reaction [27,29,26,59]. The following electrochemical description is thorough: (i) the formation of an intermediate copper oxide phase $Cu_{1-x}^{II}Cu_x^I O_{1-x/2}$ ($0 \leq x \leq 0.4$) and amor-
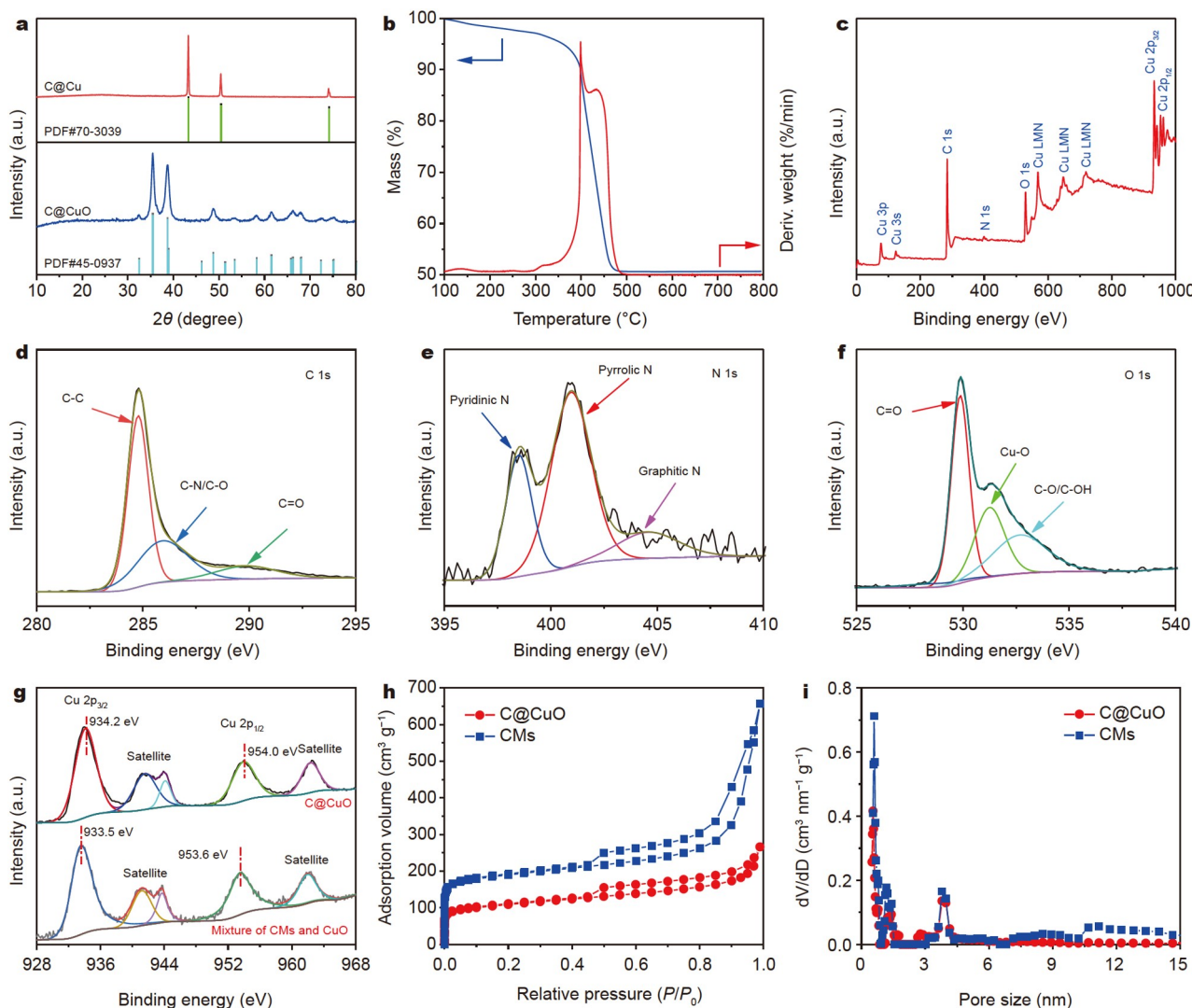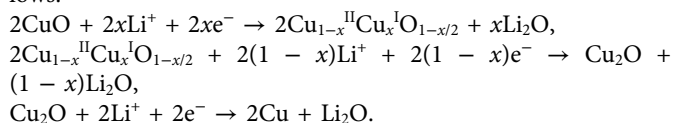
Figure 3 (a) XRD patterns of C@Cu and C@CuO, (b) TG and DTG curves of C@CuO. XPS spectra of C@CuO: (c) full survey, (d) C 1s, (e) N 1s, and (f) O 1s. (g) Cu 2p XPS spectra of C@CuO and the mixture of CMs and CuO. (h) N_2 adsorption-desorption isotherms of C@CuO and CMs, and (i) the corresponding DFT pore size distributions.

phous Li_2O; (ii) the decomposition of $Cu_{1-x}^{II}Cu_x^{I}O_{1-x/2}$ into the Cu_2O phase, which follows the formation of the solid–electrolyte interface (SEI) film; (iii) the further conversion of Cu_2O into Cu and the creation of Li_2O. Subsequently, distinct oxidation peaks were identified at 1.13 and 2.46 V, which are related to the formation of Cu_2O and the oxidation of Cu_2O to CuO, respectively [60]. In addition, the 2nd, 3rd, and 4th cycles of the CV curves almost overlapped, indicating the excellent cycling stability of the C@CuO electrode [61]. According to the above analysis, the corresponding reactions can be expressed as follows:

$2CuO + 2xLi^+ + 2xe^- \rightarrow 2Cu_{1-x}^{II}Cu_x^{I}O_{1-x/2} + xLi_2O$,

$2Cu_{1-x}^{II}Cu_x^{I}O_{1-x/2} + 2(1-x)Li^+ + 2(1-x)e^- \rightarrow Cu_2O + (1-x)Li_2O$,

$Cu_2O + 2Li^+ + 2e^- \rightarrow 2Cu + Li_2O$.

After the second cycle, the cathodic potentials were increased to approximately 0.82 and 1.36 V. Likewise, the anodic potential was moved to 2.58 V. This process is typical of structural alterations in metal oxides during charging and discharging, and the decrease in intensity and integral area of individual peaks

reflects capacity loss and the creation of SEI layers during the first cycle [62]. Thus, the highly overlapping CV curves, excluding the first cycle, demonstrated high reversibility of the redox reaction at the C@CuO electrode and excellent cycling stability due to the hierarchical pore structure. Fig. 4b shows the GCD profiles measured between 0.01 and 3.0 V at a current density of 100 mA g^{-1}. In the first discharge curve, four potential ranges are observed at 0.8–0.9, 1.0–1.1, 1.2–1.4, and 2.0–2.3 V, which can be attributed to the reaction of Li$^+$ insertion into CuO and the irreversible formation of the SEI film. Among the other discharge curves, only two discharge voltage plateaus are observed, at 0.8–0.9 and 1.3–1.4 V, which correspond to the insertion of Li$^+$ into CuO. During the charging process, two voltage plateaus are located at approximately 1.1 and 2.4 V, which are due to the recombination of Cu and Li_2O turning into CuO and Li$^+$, respectively. In addition, except for the first discharge curve, the location of the voltage plateau for subsequent discharging and charging curves remains constant, indicating that the C@CuO electrode has high structural stability and reversible electrochemical properties. We note that the plateaus
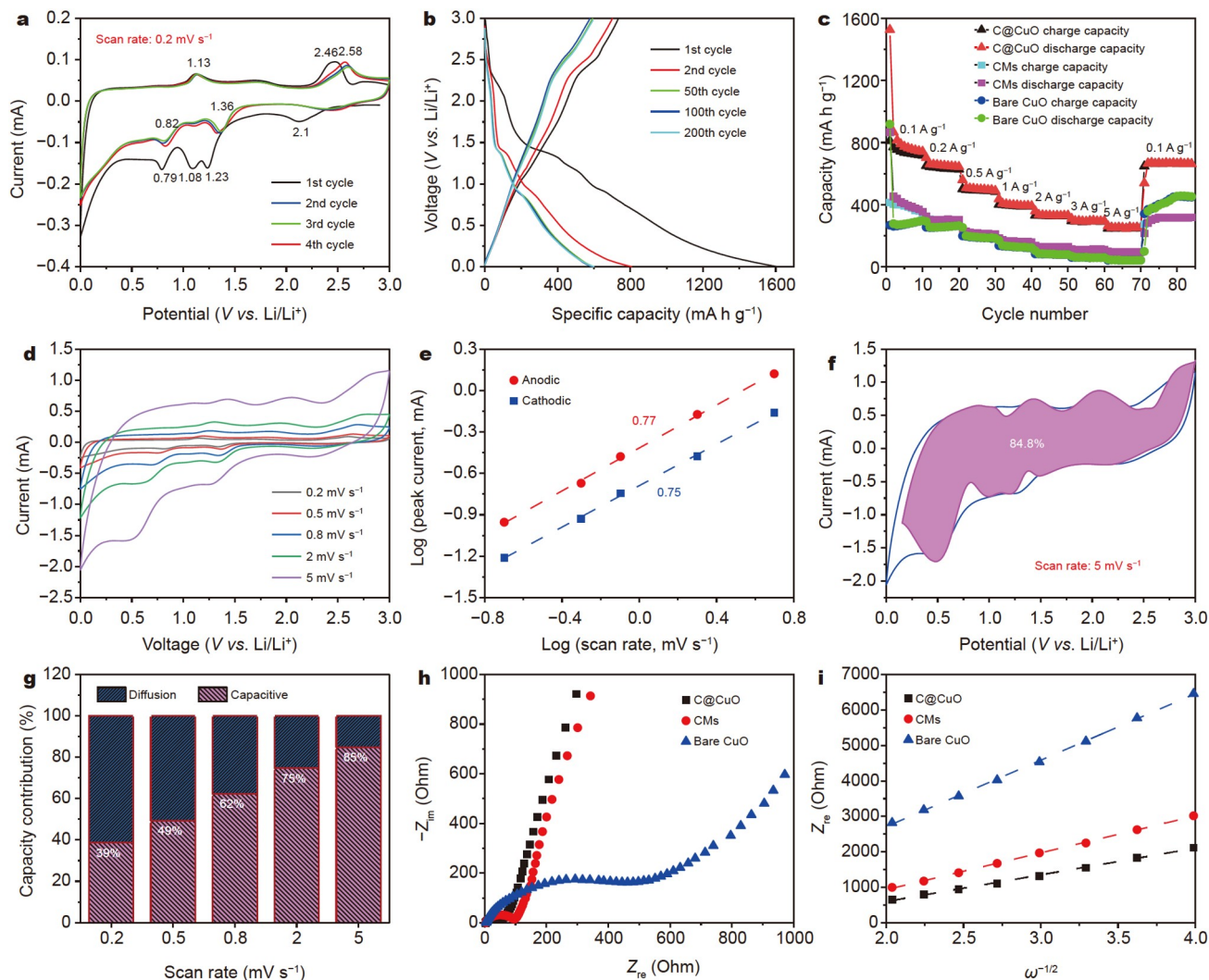
Figure 4 (a) First four CV curves of the C@CuO electrode within the potential range of 0.01–3.0 V at a scan rate of 0.2 mV s^{-1}. (b) GCD curves of the C@CuO electrode from the first to the 200th cycle at a current density of 100 mA g^{-1}. (c) Rate performances of C@CuO, CMs, and bare CuO electrodes at different current densities. (d) CV curves of C@CuO electrode at different scan rates. (e) Relationship between the peak current and the scan rate for the C@CuO electrode. (f) Capacitive contribution (pink) to charge storage at a scan rate of 5 mV s^{-1}. (g) Contributions of the diffusion-controlled and capacitive capacity of C@CuO electrode at different scan rates. (h) EIS curves of C@CuO, CMs, and bare CuO electrodes after 15 cycles, and (i) the relationship curves between real parts of the impedance (Z_{re}) of the electrodes in the low frequency region and the reciprocal square root of angular frequency ($\omega^{-1/2}$).

on the GCD profiles agree well with the CV curves.

To further comprehend the advantage of the hierarchical nanostructures in lithium storage, the relationship between specific capacity and discharge–charge rates from 100 to 5000 mA g^{-1} for the C@CuO microspheres was examined, and the results are presented in Fig. 4c. The C@CuO electrode displays the best reversible capacity and rate performance. The C@CuO electrode exhibits good capacity retention despite rapid changes in current densities. At current densities of 100, 200, 500, 1000, 2000, 3000, and 5000 mA g^{-1}, the corresponding average discharge capacities are 755, 643, 495, 396, 329, 293, and 262 mA h g^{-1}, respectively. Even after a rapid change in current density, the electrode can still recover to a discharge capacity of ~668 mA h g^{-1} when the current density is reduced to 100 mA g^{-1}, which demonstrates the strong reversibility and cycling stability of the C@CuO electrode. However, the CMs and the bare CuO electrodes have much lower average discharge capacities than the C@CuO electrode. At various current den-

sities, the charge/discharge curves of the C@CuO electrode exhibited apparent sloping platforms (Fig. S5), which is due to the diffusive and capacitive lithium storage mechanisms (Fig. S6).

To further investigate the mechanism of Li$^+$ storage in the electrode, we obtained the CV curves of the C@CuO electrode at different scan rates (Fig. 4d). As the scan rate increased, the curves remained the same shape but widened. Because of polarization, the oxidation peak in the CV curves inevitably moves upward and the reduction peak moves downward as the scan rate increases, which is due to the inevitable resistance between the current and potential [63]. After removing the polarization effect using data processing, we can use Equations (1) and (2) [46].

$$i = av^b, \tag{1}$$
$$\log(i) = b\log(v) + \log(a), \tag{2}$$

where a and b in these equations are variable constants, while i and v denote the peak current and scan rate, respectively. The

value of b can be calculated using Equation (2). If b is near 0.5, the electrochemical reactions are dominated by a diffusive mechanism. If b is near 1.0, a capacitive mechanism is obeyed. The calculated b values of 0.77 and 0.75 for the anodic and cathodic processes (Fig. 4e), respectively, suggest that the capacity of the C@CuO electrode is contributed by a combination of diffusive and capacitive mechanisms. The capacitive contribution component of the C@CuO electrode capacity can be calculated using Equations (3) and (4) [46].

$$i = k_1 v^{1/2} + k_2 v, \tag{3}$$
$$i/v^{1/2} = k_1 + k_2 v^{1/2}, \tag{4}$$

where k_1 and k_2 in these equations are constants, $k_1 v^{1/2}$ is the diffusion-controlled reaction contribution, and $k_2 v$ represents the surface-driven process contribution. Meanwhile, we can use the method introduced by Dunn's group [64] to determine the capacitive contribution by calculating the shaded region in the voltammogram. According to the shaded region in Fig. 4f, the capacitive contribution of the C@CuO electrode at a scan rate of 5.0 mV s^{-1} is 84.8%. Fig. 4g illustrates the precise capacitive contributions of the C@CuO electrode at different scan rates. The capacitive contribution of the C@CuO electrode increases progressively with increasing scan rate. Therefore, we can conclude that the capacity composition of the C@CuO electrode is dominated by the diffusive capacity at a lower scan rate. In contrast, the capacitive contribution of the C@CuO electrode is higher at high scan rates, suggesting that the unique structure of C@CuO is favorable for the surface-induced storage of Li$^+$ at high current densities. As capacitive processes are important in the rapid storage of Li$^+$, the excellent rate performance of the C@CuO electrode can be ascribed to its unique and stable structure [65].

EIS experiments were performed to evaluate the Li$^+$ diffusion kinetics and charge transfer behavior of the electrode materials. Fig. S7 shows the EIS curves of the C@CuO cells after 1, 5, and 15 cycles. In the high- and medium-frequency regions, all EIS curves exhibit a semicircle, which is due to a re-equilibration corresponding to charge transfer and SEI film resistance. In addition, in the low-frequency region, all EIS curves exhibit a linear Warburg tail, which may be ascribed to the solid-state diffusion of Li$^+$ in the electrode material [66]. Using the equivalent circuit model in Fig. S8 [67], the semicircle in the medium to high frequency range was divided into SEI resistance (R_f) and charge transfer resistance (R_{ct}), and the corresponding results are summarized in Table S2. The R_{ct} decreases from 49.2 Ω in the cell after 1 cycle to 11.3 Ω in the cell after 15 cycles, indicating a more rapid charge transfer in the cell after cycling, which may reduce polarization. Equation (5) can be used to analyze and determine the diffusion coefficient of Li$^+$ ions (D_{Li+}) for the electrodes [66].

$$D_{Li^+} = R^2 T^2 / 2A^2 n^4 F^4 C^2 \sigma^2. \tag{5}$$

The parameters and constants in this equation are T (absolute temperature), R (gas constant), C (concentration of lithium ions), n (number of electrons involved in the reaction), σ (Warburg factor), A (surface area of the electrode), and F (Faraday constant), where σ is related to Z_{re} in the low-frequency region and can be determined using Equations (6) and (7):

$$Z_{re} = R + \sigma \omega^{-1/2}, \tag{6}$$
$$\omega = 2\pi f, \tag{7}$$

where ω is the angular frequency and f is the corresponding frequency. Plots of Z_{re} versus $\omega^{-1/2}$ for C@CuO cells after 1, 5, and 15 cycles are shown in Fig. S9, which depicts a linear rela-

tionship between Z_{re} and $\omega^{-1/2}$. The D_{Li+} of the 15-cycle C@CuO electrode is approximately 2.0-fold and 1.3-fold larger than that of the one-cycle C@CuO electrode and the five-cycle C@CuO electrode, respectively. The EIS curves of the C@CuO, CMs, and bare CuO cells after 15 cycles are shown in Fig. 4h. Similarly, the equivalent circuit model in Fig. S8 can be used to obtain the R_{ct} and R_f of the electrodes, which are also collected in Table S2. The C@CuO cell has the lowest R_{ct} value (11.3 Ω) compared with the CMs (65.8 Ω) and bare CuO (388.1 Ω) cells, suggesting that it has the highest charge transfer rate. Fig. 4i shows the relationship between Z_{re} and $\omega^{-1/2}$ for the C@CuO, CMs, and bare CuO electrodes. The D_{Li+} of the C@CuO electrode is approximately 6.3- and 2.1-fold larger than that of the CMs and bare CuO electrodes, respectively. Equations (5)–(7) indicate that the lower the value of σ is, the higher the value of D_{Li}, indicating a faster transport of Li$^+$ in the C@CuO electrode [68]. Obviously, the unique structure of the C@CuO electrode is favorable for electron/ion charge transport.

The cycling performance of the C@CuO electrode was evaluated at a current density of 100 mA g^{-1} (Fig. S10). We evaluated the results of the CM and bare CuO electrodes under identical test conditions for comparison. The discharge capacity of the CM electrode decreases mildly and then increases gradually throughout the cycling process. Notably, the initial coulombic efficiency of the CM electrode is only approximately 52% because of the generation of the SEI film. The initial coulombic efficiency of the C@CuO anode can be improved by pre-lithiation, and the initial irreversible capacity loss can be compensated for by introducing a lithium supplement additive into the anode [69]. However, except for the initial two cycles, the coulombic efficiency of CMs exhibits a rapid increase and could eventually be stably maintained at approximately 99%, proving the excellent capacity retention of the CM electrode. In addition, the specific capacity of the bare CuO electrode initially shows an obvious gradual increase, followed by rapid, cliff-like decay throughout the cycling process. The gradual increase in the reversible capacity of metal oxide anode materials during charging and discharging is a common phenomenon, and it is most likely caused by the gradual activation process of the metal oxide electrode and the reversible reactions between the electrolyte and metal particles [2]. On the other hand, the inherent disadvantages of CuO lead to poor cycling stability, exhibiting rapid capacity fading. The C@CuO microspheres combine a multiscale pore structure with a rational distribution of CuO nanosheets. The C@CuO electrode still has a high reversible capacity of 626 mA h g^{-1} and a capacity retention of ~93% after 200 cycles. The long-term cycling curves are shown in Fig. 5a to assess the cycling stability of the electrodes. The specific capacity of the C@CuO electrode first mildly decreases to ~472 mA h g^{-1} and then gradually increases to ~553 mA h g^{-1} after 600 cycles. The same phenomenon is presented in the charge/discharge cycles of the CM electrode. The specific capacity of the CM electrode remained stable at ~212 mA h g^{-1} after 50 cycles. From 150 cycles onward, the specific capacity of CMs gradually increased and eventually remained stable. The specific capacity of the CM electrode after 600 cycles remained at ~261 mA h g^{-1}, accompanied by a capacity retention of ~102%. The increased capacity of the C@CuO and CM electrodes is due to the expansion of the interlayer distance of the chitin-derived carbon during charge/discharge process [70]. The bare CuO electrode delivered lower discharge and charge capacities. Similarly, the second
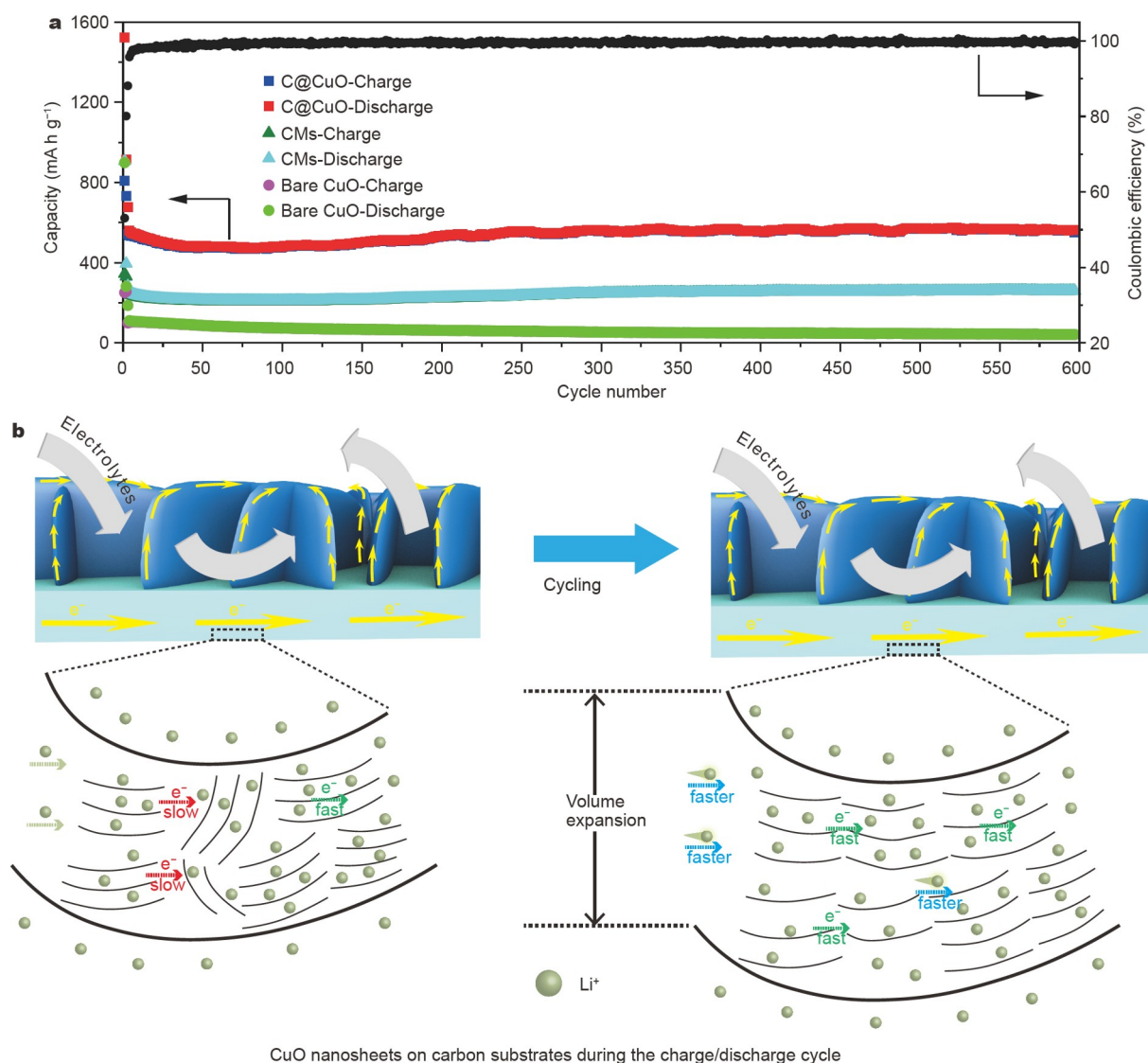
Figure 5 (a) Cycling performances and the corresponding coulombic efficiency of C@CuO, CMs, and bare CuO electrodes at 1000 mA g^{-1}. (b) Schematic of structural changes and Li$^+$ and electron transport in the C@CuO electrode before and after cycling.

discharge capacity of the bare CuO electrode was ~281 mA h g^{-1} because of the large capacity loss caused by the SEI film formation in the first cycle. In addition, the specific capacity of the CuO electrode gradually decreased with discharge/charge cycles and dropped to ~43 mA h g^{-1} after 600 cycles, with a capacity retention of ~39%. The capacity loss of the bare CuO electrode during cycling is caused by the pulverization and agglomeration of the CuO nanosheets during the continuous charge/discharge process [71].

To investigate the mechanism of capacity increase with cycling, first, XRD tests were performed to analyze the change in carbon interlayer distance after long cycling (Fig. S11a). The (002) peak of C@CuO after 600 cycles (completely delithiated) is broad, confirming its amorphous nature. The calculated interlayer distance of the (002) peak was 0.40 nm, larger than 0.37 nm for the original electrode, demonstrating that the repeated charge/discharge processes increase the interlayer distance. The enlarged carbon interlayer distance not only enhances ion transport but also accommodates more Li$^+$, thus increasing the capacity of the carbon material. Second, to examine the effect

of the high-rate charge/discharge process on the carbon structure, a cycled C@CuO electrode (completely delithiated) was investigated using Raman spectra (Fig. S11b). The results reveal no apparent alterations in the D- and G-bands even after 600 cycles, demonstrating that the chitin-derived carbon can maintain its structural integrity during prolonged cycling. The intensity ratio of D/G bands (I_D/I_G) of the electrode after 600 cycles was considerably lower than that of the original electrode, indicating that the long cycling resulted in a better alignment of the graphitic carbon layers [72,73]. Better-aligned graphite layers not only facilitate the transport of lithium ions between carbon layers but also provide better transport paths for electrons, leading to faster charge transport [74]. On the basis of the foregoing findings, we can outline the reasons for the excellent cycling stability and the increase in capacity after the long cycling of the electrodes, and the corresponding schematic is shown in Fig. 5b. The robust and interconnected multiscale pore structure can mitigate the volume expansion of the C@CuO electrode after cycling, thereby maintaining its structural integrity. Thus, based on the above properties, the C@CuO electrode

can ensure fast lithium storage from the surface-induced capacitive process, which explains the increase in capacity.

The excellent cycling stability of C@CuO is due to its unique structure. The nitrogen-doped carbon derived from chitin used as a lithium plating substrate can regulate the nucleation of lithium metal and limit dendritic crystal formation [75]. The low nucleation overpotential of CuO and the uniform Li^+ ion flux induced by CuO nanosheets on the carbon substrate can effectively prevent the generation of Li dendrites and lead to uniform Li nucleation [31,76,77]. The mechanism of the Li nucleation and deposition process on bare CuO and C@CuO is shown in Fig. 6. For the bare CuO electrode (Fig. 6a), during the lithiation process, Li particles usually aggregate into irregular island-like shapes with the presence of dendritic Li and mossy Li on the surface. After repeated lithiation and de-lithiation processes, isolated lithium and dead lithium are continuously generated on the electrode surface, forming an unstable interface that greatly limits Li^+ transfer and leads to poor coulombic efficiency and rapid capacity decay [78]. In contrast, as shown in Fig. 6b, the nitrogen-doped carbon substrate and the uniformly grown CuO nanosheets provide abundant Li nucleation sites. Therefore, Li can be nucleated and grown on the surface of carbon substrates and CuO nanosheets, promoting the uniform deposition of Li. The C@CuO microspheres possessed a multiscale porous structure with uniformly distributed CuO nanosheets as the anode material for LIBs, which not only has excellent structural stability during cycling but also can reduce the local effective current density, thus forming a uniform electric field for uniform Li deposition. Finally, the C@CuO electrode was obtained with homogeneous Li deposition and dendrite-free morphology. Fig. 6c, d show the SEM images of the bare CuO and C@CuO electrodes, respectively, in the half-cells after cycling. As depicted in Fig. 6c, after 200 cycles at 100 mA g^{-1}, a rough island-like Li aggregate is observed on the bare CuO electrode and has

randomly dispersed mossy Li on its surface. This morphology of Li deposition arises from the inhomogeneous lithiation and delithiation occurring on the bare CuO electrode [75,76]. Importantly, the nitrogen-doped carbon substrates and CuO nanosheets provided plentiful Li nucleation sites on the C@CuO electrode, facilitating the subsequent Li deposition process. As shown in Fig. 6d, after 200 cycles at 100 mA g^{-1}, Li was deposited almost uniformly on the surface of the C@CuO electrode, forming a relatively smooth Li layer. In addition, the nucleation overpotential was used to quantitatively assess the degree of lithiophilicity on the electrode surface. The Li nucleation overpotential is a key parameter for evaluating the barrier to heterogeneous Li formation by electrochemical plating, and it is defined as the difference between the initial Li plating mutation potential and the subsequent Li deposition stability potential [75]. As shown in Fig. S12, a sharp voltage drop to −0.205 V was recorded at the beginning of the Li plating process on the bare CuO electrode, which was associated with the nucleation process of metallic Li. After nucleation, a plateau corresponding to Li growth was observed near −0.086 mV, thus giving a nucleation overpotential of 0.119 V. In contrast, the C@CuO electrode exhibited an inclined voltage drop to −0.074 V and stabilized at −0.028 V, achieving a lower nucleation overpotential of 0.046 V compared with the bare CuO electrode. The above results show that the C@CuO electrode can reduce the nucleation overpotential and achieve the uniform nucleation and growth of Li.

As summarized in Fig. S13 and Table S3, the electrochemical performance of the C@CuO microspheres was compared with those of other reported CuO and CuO-based electrodes with various morphologies. The C@CuO electrode prepared in this study exhibited high reversible specific capacity and remarkable cycling stability capability in lithium-ion storage, being one of the best performances among all CuO-based anode materials for
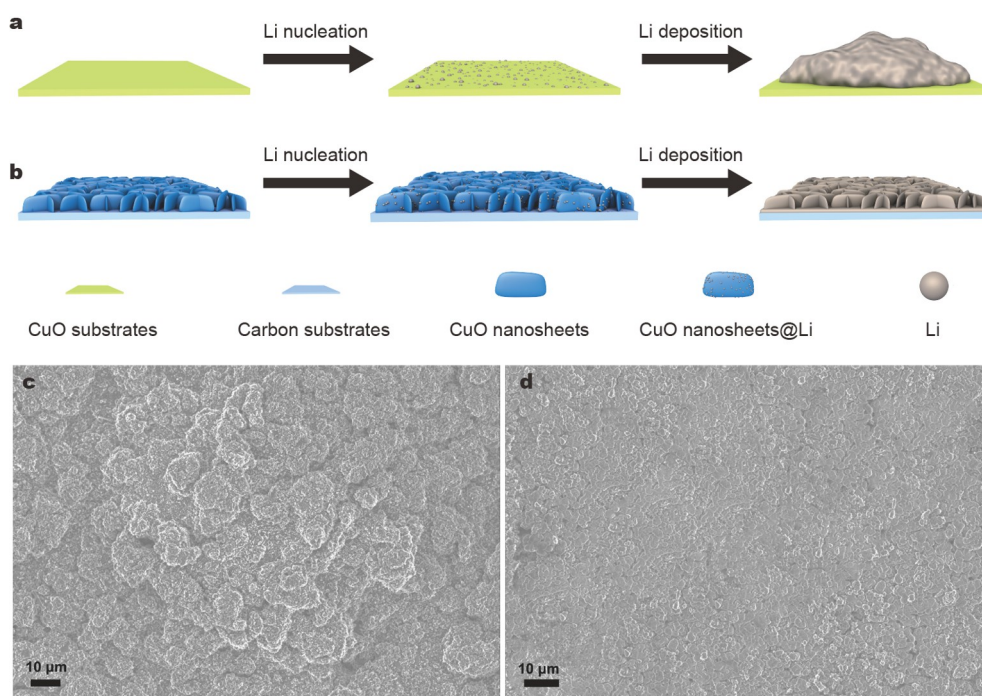

Figure 6 Schematics of the Li nucleation and deposition processes on (a) bare CuO and (b) C@CuO. SEM images of Li plating on (c) bare CuO and (d) C@CuO after 200 cycles at 100 mA g^{-1}.

LIBs. This performance benefits from the co-effect between porous CMs and uniformly dispersed CuO nanosheets. First, the interpenetrating micro/meso/macroporous structure of C@CuO microspheres has a high specific surface area, which not only ensures the effective penetration of the electrolyte and improves the contact area between the electrolyte and electrode but also shortens the ion transport length. Second, the C@CuO microsphere, with a multiscale porous structure and adequate space between the CuO nanosheets, can alleviate the volume expansion caused by the Li^+ insertion and extraction reactions and prevent the nanostructures from agglomerating. Third, the high specific surface area of nitrogen-doped CMs and uniformly distributed CuO nanosheets not only provide a substantial amount of nucleation sites for Li but also contribute to the uniform nucleation and homogeneous growth of Li. Thus, the C@CuO electrode exhibits outstanding electrochemical performance.

CONCLUSIONS

In summary, we developed CMs with hierarchical structures and self-grown CuO nanosheets as anode materials for LIBs. The prepared C@CuO microspheres exhibit an interconnected multiscale pore structure, which facilitates the diffusion of electrolyte, increases the contact area between the electrode and electrolyte, promotes the charge transfer, and buffers the volume expansion of the electrode during charging and discharging. Moreover, the nitrogen-doped chitin-derived carbon substrates and CuO nanosheets not only provide abundant lithium nucleation sites but also induce the homogeneous nucleation and growth of Li. Thus, when used as LIB anode materials, the resulting C@CuO electrode delivers superior cycling stability and outstanding reversible capacity (626 mA h g^{-1} after 200 cycles at a current density of 100 mA g^{-1} with a capacity retention of ~93% and 553 mA h g^{-1} after 600 cycles at a current density of 1000 mA g^{-1}). This excellent electrochemical performance ensures that C@CuO microspheres are potential anode materials for LIBs. Therefore, this study provides an innovative idea for the rational development of 3D carbon/metal (transition metal oxide) hybrids that can be used to develop high-performance energy storage devices.

1 Chen Z, Danilov DL, Eichel RA, *et al.* Porous electrode modeling and its applications to Li-ion batteries. Adv Energy Mater, 2022, 12: 2201506

2 Dang R, Jia X, Liu X, *et al.* Controlled synthesis of hierarchical Cu nanosheets@CuO nanorods as high-performance anode material for lithium-ion batteries. Nano Energy, 2017, 33: 427–435

3 Chen X, Li H, Yan Z, *et al.* Structure design and mechanism analysis of silicon anode for lithium-ion batteries. Sci China Mater, 2019, 62: 1515–1536

4 Mohamed HSH, Wu L, Li CF, *et al. In-situ* growing mesoporous CuO/O-doped g-C_3N_4 nanospheres for highly enhanced lithium storage. ACS Appl Mater Interfaces, 2019, 11: 32957–32968

5 Chen Z, Hou Z, Xu W, *et al.* Ultrafine CuO nanoparticles decorated activated tube-like carbon as advanced anode for lithium-ion batteries. Electrochim Acta, 2019, 296: 206–213

6 Kong L, Liu Y, Huang H, *et al.* Interconnected CoS_2/NC-CNTs network as high-performance anode materials for lithium-ion batteries. Sci China Mater, 2021, 64: 820–829

7 Zhu K, Sun Y, Wang R, *et al.* Fast synthesis of uniform mesoporous titania submicrospheres with high tap densities for high-volumetric performance Li-ion batteries. Sci China Mater, 2017, 60: 304–314

8 Wang G, Gao W, Zhan Z, *et al.* Defect-engineered TiO_2 nanocrystals for enhanced lithium-ion battery storage performance. Appl Surf Sci, 2022, 598: 153869

9 Shi Y, Pan X, Li B, *et al.* Co_3O_4 and its composites for high-performance Li-ion batteries. Chem Eng J, 2018, 343: 427–446

10 Sun Y, Huang F, Li S, *et al.* Novel porous starfish-like Co_3O_4@nitrogen-doped carbon as an advanced anode for lithium-ion batteries. Nano Res, 2017, 10: 3457–3467

11 Zhou Y, Wang C, Chen F, *et al.* Synchronous constructing ion channels and confined space of Co_3O_4 anode for high-performance lithium-ion batteries. Nano Res, 2022, 15: 6192–6199

12 Yuan X, Ma Z, Jian S, *et al.* Mesoporous nitrogen-doped carbon MnO_2 multichannel nanotubes with high performance for Li-ion batteries. Nano Energy, 2022, 97: 107235

13 Liu H, Wang JG, Hua W, *et al.* Scale-up production of high-tap-density carbon/MnO_x/carbon nanotube microcomposites for Li-ion batteries with ultrahigh volumetric capacity. Chem Eng J, 2018, 354: 220–227

14 Xu D, Mu C, Wang B, *et al.* Fabrication of multifunctional carbon encapsulated Ni@NiO nanocomposites for oxygen reduction, oxygen evolution and lithium-ion battery anode materials. Sci China Mater, 2017, 60: 947–954

15 Ata-ur-Rehman , Iftikhar M, Latif S, *et al.* Current advances and prospects in NiO-based lithium-ion battery anodes. Sustain Energy Techn Assess, 2022, 53: 102376

16 Wu K, Ling M, Zeng P, *et al.* Self-assembled multifunctional Fe_3O_4 hierarchical microspheres: High-efficiency lithium-ion battery materials and hydrogenation catalysts. Sci China Mater, 2020, 64: 1058–1070

17 Wang Y, Chen L, Liu H, *et al.* Cornlike ordered N-doped carbon coated hollow Fe_3O_4 by magnetic self-assembly for the application of Li-ion battery. Chem Eng J, 2019, 356: 746–755

18 Zhou J, Xu S, Kang Q, *et al.* Iron oxide encapsulated in nitrogen-rich carbon enabling high-performance lithium-ion capacitor. Sci China Mater, 2020, 63: 2289–2302

19 Min X, Sun B, Chen S, *et al.* A textile-based SnO_2 ultra-flexible electrode for lithium-ion batteries. Energy Storage Mater, 2019, 16: 597–606

20 Zhu Y, Cao T, Li Z, *et al.* Two-dimensional SnO_2/graphene heterostructures for highly reversible electrochemical lithium storage. Sci China Mater, 2018, 61: 1527–1535

21 Xu C, Manukyan KV, Adams RA, *et al.* One-step solution combustion synthesis of CuO/Cu_2O/C anode for long cycle life Li-ion batteries. Carbon, 2019, 142: 51–59

22 Dong Y, Jiang X, Mo J, *et al.* Hollow CuO nanoparticles in carbon microspheres prepared from cellulose-cuprammonium solution as anode materials for Li-ion batteries. Chem Eng J, 2020, 381: 122614

23 Yin D, Huang G, Na Z, *et al.* CuO nanorod arrays formed directly on Cu foil from MOFs as superior binder-free anode material for lithium-ion batteries. ACS Energy Lett, 2017, 2: 1564–1570

24 Ji D, Zhou H, Tong Y, *et al.* Facile fabrication of MOF-derived octahedral CuO wrapped 3D graphene network as binder-free anode for high performance lithium-ion batteries. Chem Eng J, 2017, 313: 1623–1632

25 Mishra SR, Ahmaruzzaman M. CuO and CuO-based nanocomposites: Synthesis and applications in environment and energy. Sustain Mater Technologies, 2022, 33: e00463

26 Mallakpour S, Azadi E, Mustansar Hussain C. Environmentally benign production of cupric oxide nanoparticles and various utilizations of their polymeric hybrids in different technologies. Coord Chem Rev, 2020, 419: 213378

27 Kim J, Jang W, Kim JH, *et al.* Synthesis of graphene quantum dots-coated hierarchical CuO microspheres composite for use as binder-free anode for lithium-ion batteries. Compos Part B-Eng, 2021, 222: 109083

28 Jia S, Wang Y, Liu X, *et al.* Hierarchically porous CuO nano-labyrinths as binder-free anodes for long-life and high-rate lithium ion batteries. Nano Energy, 2019, 59: 229–236

29 Liu Y, Xiong L, Li P, *et al.* Self-supported CuO nanoflake arrays on nanoporous Cu substrate as high-performance negative-electrodes for lithium-ion batteries. J Power Sources, 2019, 428: 20–26

30 Yuan W, Qiu Z, Chen Y, *et al.* A binder-free composite anode composed of CuO nanosheets and multi-wall carbon nanotubes for high-performance lithium-ion batteries. Electrochim Acta, 2018, 267: 150–160

31 Zhang C, Lv W, Zhou G, *et al.* Vertically aligned lithiophilic CuO nanosheets on a Cu collector to stabilize lithium deposition for lithium metal batteries. Adv Energy Mater, 2018, 8: 1703404

32 Wang L, Gong H, Wang C, *et al.* Facile synthesis of novel tunable highly porous CuO nanorods for high rate lithium battery anodes with realized long cycle life and high reversible capacity. Nanoscale, 2012, 4: 6850–6855

33 Sahay R, Suresh Kumar P, Aravindan V, *et al.* High aspect ratio electrospun CuO nanofibers as anode material for lithium-ion batteries with superior cycleability. J Phys Chem C, 2012, 116: 18087–18092

34 Yang W, Wang J, Ma W, *et al.* Free-standing CuO nanoflake arrays coated Cu foam for advanced lithium ion battery anodes. J Power Sources, 2016, 333: 88–98

35 Huang J, Zhu Y, Yang X, *et al.* Flexible 3D porous CuO nanowire arrays for enzymeless glucose sensing: *In situ* engineered *versus ex situ* piled. Nanoscale, 2015, 7: 559–569

36 Yuan W, Luo J, Pan B, *et al.* Hierarchical shell/core CuO nanowire/carbon fiber composites as binder-free anodes for lithium-ion batteries. Electrochim Acta, 2017, 241: 261–271

37 Cao K, Liu H, Li W, *et al.* CuO nanoplates for high-performance potassium-ion batteries. Small, 2019, 15: 1901775

38 Liu H, Liu X, Li W, *et al.* Porous carbon composites for next generation rechargeable lithium batteries. Adv Energy Mater, 2017, 7: 1700283

39 Zhang A, Fang Z, Tang Y, *et al.* Inorganic gel-derived metallic frameworks enabling high-performance silicon anodes. Nano Lett, 2019, 19: 6292–6298

40 Huang A, Ma Y, Peng J, *et al.* Tailoring the structure of silicon-based materials for lithium-ion batteries *via* electrospinning technology. eScience, 2021, 1: 141–162

41 Pu F, Kong C, Lv J, *et al.* CuO ultrathin nanosheets decorated reduced graphene oxide as a high performance anode for lithium-ion batteries. J Alloys Compd, 2019, 805: 355–362

42 Mohamed HSH, Li CF, Wu L, *et al.* Growing ordered CuO nanorods on 2D Cu/g-C$_3$N$_4$ nanosheets as stable freestanding anode for outstanding lithium storage. Chem Eng J, 2021, 407: 126941

43 Xiao S, Pan D, Wang L, *et al.* Porous CuO nanotubes/graphene with sandwich architecture as high-performance anodes for lithium-ion batteries. Nanoscale, 2016, 8: 19343–19351

44 Gao L, Ma J, Li S, *et al.* 2D ultrathin carbon nanosheets with rich N/O content constructed by stripping bulk chitin for high-performance sodium ion batteries. Nanoscale, 2019, 11: 12626–12636

45 Gao L, Zhang G, Cai J, *et al.* Rationally exfoliating chitin into 2D hierarchical porous carbon nanosheets for high-rate energy storage. Nano Res, 2020, 13: 1604–1613

46 Zhang K, He Q, Xiong F, *et al.* Active sites enriched hard carbon porous nanobelts for stable and high-capacity potassium-ion storage. Nano Energy, 2020, 77: 105018

47 Gao L, Xiong L, Xu D, *et al.* Distinctive construction of chitin-derived hierarchically porous carbon microspheres/polyaniline for high-rate supercapacitors. ACS Appl Mater Interfaces, 2018, 10: 28918–28927

48 Zhang K, Xiong F, Zhou J, *et al.* Universal construction of ultrafine metal oxides coupled in N-enriched 3D carbon nanofibers for high-performance lithium/sodium storage. Nano Energy, 2020, 67: 104222

49 Duan B, Zheng X, Xia Z, *et al.* Highly biocompatible nanofibrous microspheres self-assembled from chitin in NaOH/urea aqueous solution as cell carriers. Angew Chem Int Ed, 2015, 54: 5152–5156

50 Shi Z, Du R, Yu C, *et al.* Graphene oxide/Cu(OH)$_2$ composites as efficient multifunctional hosts for lithium-sulfur batteries. J Alloys Compd, 2022, 925: 166642

51 Ren H, Yu R, Qi J, *et al.* Hollow multishelled heterostructured anatase/TiO$_2$(B) with superior rate capability and cycling performance. Adv Mater, 2019, 31: 1805754

52 Dong Y, Jia B, Fu F, *et al.* Fabrication of hollow materials by fast pyrolysis of cellulose composite fibers with heterogeneous structures. Angew Chem Int Ed, 2016, 55: 13504–13508

53 Zou G, Hou H, Foster CW, *et al.* Advanced hierarchical vesicular carbon co-doped with S, P, N for high-rate sodium storage. Adv Sci, 2018, 5: 1800241

54 Yang J, Ju Z, Jiang Y, *et al.* Enhanced capacity and rate capability of nitrogen/oxygen dual-doped hard carbon in capacitive potassium-ion storage. Adv Mater, 2018, 30: 1700104

55 Wu P, Fang Z, Zhang A, *et al.* Chemically binding scaffolded anodes with 3D graphene architectures realizing fast and stable lithium storage. Research, 2019, 2019

56 Xu C, Xia T, Wang C, *et al.* Stable and fast Si–M–C ternary anodes enabled by interfacial engineering. J Power Sources, 2022, 530: 231290

57 Cheng Q, Huang M, Xiao A, *et al.* Recyclable nitrogen-containing chitin-derived carbon microsphere as sorbent for neonicotinoid residues adsorption and analysis. Carbohydrate Polyms, 2021, 260: 117770

58 Shao J, Song M, Wu G, *et al.* 3D carbon nanocage networks with multiscale pores for high-rate supercapacitors by flower-like template and *in-situ* coating. Energy Storage Mater, 2018, 13: 57–65

59 Yuan W, Luo J, Yan Z, *et al.* High-performance CuO/Cu composite current collectors with array-pattern porous structures for lithium-ion batteries. Electrochim Acta, 2017, 226: 89–97

60 Wang C, Li Q, Wang F, *et al.* Morphology-dependent performance of CuO anodes *via* facile and controllable synthesis for lithium-ion batteries. ACS Appl Mater Interfaces, 2014, 6: 1243–1250

61 Yang S, Wang S, Liu X, *et al.* Biomass derived interconnected hierarchical micro-meso-macro- porous carbon with ultrahigh capacitance for supercapacitors. Carbon, 2019, 147: 540–549

62 Pu F, Bai Y, Lv J, *et al.* Yolk-shell Cu$_2$O@CuO-decorated RGO for high-performance lithium-ion battery anode. Energy Environ Mater, 2021, 5: 253–260

63 Pu X, Zhao D, Fu C, *et al.* Understanding and calibration of charge storage mechanism in cyclic voltammetry curves. Angew Chem Int Ed, 2021, 60: 21310–21318

64 Brezesinski T, Wang J, Polleux J, *et al.* Templated nanocrystal-based porous TiO$_2$ films for next-generation electrochemical capacitors. J Am Chem Soc, 2009, 131: 1802–1809

65 Li S, Qiu J, Lai C, *et al.* Surface capacitive contributions: Towards high rate anode materials for sodium ion batteries. Nano Energy, 2015, 12: 224–230

66 Ni D, Sun W, Wang Z, *et al.* Heteroatom-doped mesoporous hollow carbon spheres for fast sodium storage with an ultralong cycle life. Adv Energy Mater, 2019, 9: 1900036

67 Deng X, Xie K, Li L, *et al.* Scalable synthesis of self-standing sulfur-doped flexible graphene films as recyclable anode materials for low-cost sodium-ion batteries. Carbon, 2016, 107: 67–73

68 Guo R, Lv C, Xu W, *et al.* Effect of intrinsic defects of carbon materials on the sodium storage performance. Adv Energy Mater, 2020, 10: 1903652

69 Shen Y, Qian J, Yang H, *et al.* Chemically prelithiated hard-carbon anode for high power and high capacity Li-ion batteries. Small, 2020, 16: 1907602

70 Liu Y, Yan X, Yu Y, *et al.* Self-improving anodes for lithium-ion batteries: Continuous interlamellar spacing expansion induced capacity increase in polydopamine-derived nitrogen-doped carbon tubes during cycling. J Mater Chem A, 2015, 3: 20880–20885

71 Zhang J, Yu A. Nanostructured transition metal oxides as advanced anodes for lithium-ion batteries. Sci Bull, 2015, 60: 823–838

72 Xiao W, Sun Q, Liu J, *et al.* Utilizing the full capacity of carbon black as anode for Na-ion batteries *via* solvent co-intercalation. Nano Res, 2017, 10: 4378–4387

73 Qian J, Wu F, Ye Y, *et al.* Boosting fast sodium storage of a large-scalable carbon anode with an ultralong cycle life. Adv Energy Mater, 2018, 8: 1703159

74 Yu ZL, Xin S, You Y, *et al.* Ion-catalyzed synthesis of microporous hard carbon embedded with expanded nanographite for enhanced lithium/sodium storage. J Am Chem Soc, 2016, 138: 14915–14922

75 Zhang R, Chen XR, Chen X, *et al.* Lithiophilic sites in doped graphene guide uniform lithium nucleation for dendrite-free lithium metal anodes. Angew Chem Int Ed, 2017, 56: 7764–7768

76 Wu S, Zhang Z, Lan M, *et al.* Lithiophilic Cu-CuO-Ni hybrid structure: Advanced current collectors toward stable lithium metal anodes. Adv Mater, 2018, 30: 1705830

77 Qiu X, Yu M, Fan G, *et al.* Growing nanostructured CuO on copper foil *via* chemical etching to upgrade metallic lithium anode. ACS Appl Mater Interfaces, 2021, 13: 6367–6374

78 Cheng Y, Ke X, Chen Y, *et al.* Lithiophobic-lithiophilic composite architecture through co-deposition technology toward high-performance lithium metal batteries. Nano Energy, 2019, 63: 103854

Author contributions Sun X conceived the idea and designed the experiments. Sun X and Wang Z carried out all experiments. Sun X and Zhou J analyzed the data and wrote the original draft. Ai X and Zhou J reviewed and edited the manuscript. Zhou J supervised the project.

Conflict of interest The authors declare that they have no conflict of interest.

Supplementary information Supporting data are available in the online version of the paper.

Xun Sun received his MS degree in polymer chemistry and physics from Fujian Normal University in 2018. He is currently pursuing his PhD degree at Wuhan University, where his current research focuses on natural polymeric materials for energy storage and conversion.

Zhe Wang received his Bachelor's degree (2021) in chemistry from Wuhan University, and now studies for a Master's degree at Wuhan University. His research interests mainly focus on anode materials of LIB and pre-lithification technology.

Xinping Ai received his PhD degree (1995) in chemistry from Wuhan University, and now works as a professor at the College of Chemistry and Molecular Sciences, Wuhan University. His research interests mainly focus on electrochemical energy-storage materials and technologies.

Jinping Zhou is a professor at the College of Chemistry and Molecular Sciences, Wuhan University. He received his PhD degree in 2001 from the Department of Chemistry, Wuhan University. His research interests mainly focus on green methods for the modification and fiber spinning of cellulose, and functional materials based on natural polymers.

碳微球负载CuO纳米片用作锂离子电池的高性能负极材料

孙逊†, 王喆†, 艾新平*, 周金平*

摘要 氧化铜(CuO)具有高理论容量、丰富的资源以及生态友好等特点, 被认为是一种理想的锂离子电池负极材料. 然而, 由于CuO本身的低导电性和循环时巨大的体积膨胀, 它在电池应用中的容量利用率和循环稳定性仍然存在不足. 本工作中, 我们通过在甲壳素衍生的碳微球的内外壁上直接原位合成CuO纳米片, 构造出一种三维多孔碳@CuO复合材料. 得益于碳微球的三维多孔导电框架和CuO纳米片的合理分布, CuO的容量利用率和结构稳定性在充电/放电过程中得到明显改善, 所制备的电极具有优越的循环稳定性和出色的可逆容量. 本工作为合理设计三维碳/过渡金属氧化物杂化体并用作电池负极材料提供了新的思路.